SC-EKF-MIO: Magnetic-Inertial Odometry Based on Stochastic Clone Extended Kalman Filter

Jiazhu Li, Jian Kuang, Yan Wang, and Xiaoji Niu, *Member, IEEE*

***Abstract*—Odometry is a critical technology for autonomous navigation and localization, whether for pedestrians or other mobile platforms. However, existing odometry solutions rarely deliver high accuracy, low cost, and strong robustness all at once. In this article, we propose a magnetic-inertial odometry (MIO) method based on a magnetometer array and inertial sensors. Our approach first establishes the relationship between the platform's relative pose changes and a local magnetic-field model, then employs a stochastic clone extended Kalman filter (SC-EKF) to fuse magnetic and inertial measurements for continuous correction of the inertial navigation system (INS). Furthermore, we introduce magnetic-vector constraints to address the unobservability of absolute heading and reduce position drift errors. In typical indoor environments, such as offices and underground parking lots, our method achieves an average horizontal position RMSE of 2.5 m and a velocity estimation accuracy of up to 0.07 m/s. On publicly available datasets used by the latest state-of-the-art methods, it yields a position accuracy improvement of about 60% and velocity accuracy improvement of about 38%.**

***Index Terms*—Indoor positioning, magnetic-field-based localization, magnetometer array, MEMS-inertial measurement unit (IMU), odometry, stochastic clone extended Kalman filter (SC-EKF).**

NOMENCLATURE

b_i	Body frame at the current time instant.
b_j	Body frame at the previous time instant.
$\boldsymbol{r}$	Position vector from the origin of the magnetic-field model to an arbitrary point in space.
$\boldsymbol{\mu}$	Coefficient vector of the magnetic-field polynomial model.
$\boldsymbol{\theta}$	Magnetic-field model parameter vector after eliminating redundant parameters.
$\boldsymbol{\Phi}$	Coefficient matrix constructed from spatial terms $\boldsymbol{r}$.
$\boldsymbol{l}^{b_i}$	Coordinate vector of the magnetometer in the b_i frame.
$\boldsymbol{M}^{b_i}$	Observation vector of the magnetometer array in the b_i frame.
$\hat{\boldsymbol{M}}_j^{b_i}$	Predicted magnetic field at the previous time instant based on the magnetic-field model.
$\boldsymbol{C}_j^i$	Relative rotation matrix between the b_i and b_j frames.
$\Delta\boldsymbol{r}^{b_i}$	Position variation vector in the b_i frame.
Δt	Time interval for IMU propagation.
dt	Time interval between two magnetic array updates.
$\boldsymbol{n}_v$	Observation noise of the magnetometer array.
$\boldsymbol{n}_m$	Magnetometer measurement noise.
$\boldsymbol{C}_n^b$	Rotation matrix from the navigation frame to the body frame.

Received 7 August 2025; revised 3 November 2025; accepted 24 November 2025. Date of publication 16 December 2025; date of current version 26 December 2025. This work was supported in part by the National Key Research and Development Program of China under Grant 2024YFB3909200 and Grant 2023YFC3604704. The Associate Editor coordinating the review process was Dr. Min Xia. *(Corresponding author: Jian Kuang.)*

Jiazhu Li is with the GNSS Research Center and the School of Geodesy and Geomatics, Wuhan University, Wuhan, Hubei 430072, China (e-mail: lijiazhu@whu.edu.cn).

Jian Kuang and Yan Wang are with the GNSS Research Center and Hubei Technology Innovation Center for Spatiotemporal Information and Positioning Navigation, Wuhan University, Wuhan, Hubei 430072, China (e-mail: kuang@whu.edu.cn; wystephen@whu.edu.cn).

Xiaoji Niu is with the GNSS Research Center and Hubei Technology Innovation Center for Spatiotemporal Information and Positioning Navigation, Wuhan University, Wuhan, Hubei 430072, China, and also with Hubei Luojia Laboratory, Wuhan, Hubei 430072, China (e-mail: xjniu@whu.edu.cn).

Digital Object Identifier 10.1109/TIM.2025.3644556

I. INTRODUCTION

RELIABLE navigation and positioning under degraded or denied GNSS conditions has garnered increasing attention among researchers. A central challenge is achieving stable, autonomous localization, i.e., enabling the platform to determine its position and orientation over time without relying on external aids [1]. Dead reckoning (DR) estimates the current position by propagating a known starting position using velocity and heading measurements over time. An inertial navigation system (INS) employs an inertial measurement unit (IMU) to continuously measure acceleration and rotation rates [2]. By integrating these measurements, the INS performs a form of DR to provide continuous position, velocity, and attitude estimates. This allows INS to maintain short-term localization when GNSS signals are unavailable or jammed. However, consumer-grade devices typically use low-cost MEMS-IMUs, which exhibit limited accuracy and rapid error growth under conventional strap-down algorithms. Therefore, enhancing MEMS-IMU usability and reliability in DR requires high-precision, robustness-enhanced odometry information to constrain and mitigate inertial error growth.

Existing odometry approaches include inertial, wheel, visual, and LiDAR-based methods [1]. Each modality risks degraded performance under certain operational conditions. As mentioned above, Inertial odometry suffers from positioning drift caused by sensor bias accumulation and noise, leading to progressive error growth [3]; wheel odometry is vulnerable to

wheel slippage and terrain irregularities, which introduce nonholonomic constraint violations in motion estimation; visual odometry is highly sensitive to illumination changes and dynamic occlusions, often failing in low-texture environments [4]; and LiDAR odometry is costly, computationally intensive, and degrades in environments with weak geometric features [5].

Many published studies have discussed the shortcomings of visual odometry and SLAM methods in dynamic environments from various perspectives [6], [7], [8], [9]. For example, Xue et al. [6] presents an NGIG-based adaptive Kalman filtering framework to handle the mismatch between a fixed measurement noise covariance matrix (MNCM) and the actual measurement noise. The tightly coupled visual–inertial SLAM system in [7] does not simply remove dynamic objects; instead, it extracts feature points on moving objects and uses them as constraints to improve localization accuracy. Zhang et al. [8] builds on ORB-SLAM3 by adding a parallel moving-probability propagation thread that estimates, for each feature point, the probability of being static or dynamic, and then selects or weights feature points according to these probabilities to avoid erroneous matches. Zhang et al. [9] replaces the conventional ORB/BRIEF pipeline with lightweight deep feature extraction, fast dynamic object association, and an online binary BoW loop-closure detector, thereby improving self-localization and dynamic object tracking in high-speed and low-texture scenarios. Although these advances yield improvements under specific conditions, feature-point-based methods remain intrinsically susceptible to extreme environmental disturbances, which impede accurate and robust localization in entirely unknown environments. No existing odometry method achieves optimal precision, cost-effectiveness, and robustness simultaneously. In contrast, magnetic-field odometry provides a lightweight velocity estimate based on relatively stable magnetic signals and does not depend on a preconstructed magnetic-field map. It utilizes measurements from a magnetometer array to provide odometric information such as position or velocity [10]. While not intended to replace visual or LiDAR SLAM in their primary domains, it can serve as a useful auxiliary or backup solution in specific scenarios. For example, in indoor areas with significant magnetic-field signatures or where optical and range sensors temporarily lose tracking, magnetic-field odometry is desired to enhance the overall robustness of a multisensor navigation system.

Due to ferromagnetic interference, indoor magnetic fields exhibit long-term stability and spatial distinctiveness, making them a reliable positioning source. Vissiére et al. [11], [12] pioneered the use of indoor magnetic-field disturbances to improve IMU-based position and velocity estimation. Vissiére et al. derived equations relating magnetic-field gradients to user velocity and employed a distributed magnetometer array for velocity estimation. Subsequent studies expanded on this work [13], [14], [15]. Dorveaux [14] addressed moving rigid-body localization by integrating magnetic disturbances with IMU measurements, establishing the magnetic-inertial navigation (MINAV) framework. Chesneau et al. [15] integrated inertial sensor and multimagnetometer measurements, developing an extended Kalman filter (EKF) for data fusion. Fan et al. [16], [17] introduced a Monte Carlo-based baseline optimization for scalar magnetometer arrays, enhancing localization accuracy by maximizing signal-to-noise ratio through cross-structured array design. Zmitri et al. [18] derived higher-order differential equations of magnetic fields to mitigate noise in gradient measurements, using a distributed magnetometer array to monitor both fields and their spatial derivatives. Recent studies have applied a polynomial model to characterize local magnetic fields [19]. Further analysis of this model-based methodology is presented in [20]. They augmented the magnetic-field model parameters into the INS error-state vector to facilitate Kalman filter prediction and update processes. Detailed derivations and analyses were subsequently documented in [10], accompanied by real-world data collection to evaluate algorithm performance. The corresponding experimental datasets and implementation code were also made publicly available. These approaches rely heavily on precise estimation or matching of magnetic-field gradients. However, gradient computation and higher-order differentiation are highly susceptible to measurement noise. More critically, they fail to address the unobservability of absolute heading. In current state-of-the-art ESKF frameworks, the inclusion of a magnetic-field model introduces substantial errors when the model order is insufficient to capture field complexity; conversely, adopting higher-order models increases the state vector dimension, which is detrimental to filter performance.

Recently, a dual-magnetometer velocity estimation algorithm was implemented for robotic speed determination [21], employing waveform matching between paired vehicle-mounted magnetometers to compute forward velocity. Experimental results indicate that the approach in [21] matches wheel odometry performance in magnetically rich environments. Building on this concept, Liu et al. [22] deployed a dual-magnetometer velocity measurement system on pedestrian helmets and incorporated postural changes into the waveform similarity analysis. However, these methods rely on magnetometers mounted at the front and rear, making them suitable only for forward motion and not lateral movement. Moreover, because forward velocity is calculated by matching measurements from the front and rear magnetometers, the approach is highly sensitive to the lever arm's projection onto the horizontal plane.

To overcome the limitations of existing methods, this article presents a magnetic-inertial odometry (MIO) approach based on a magnetometer array and inertial sensors. We begin with the local magnetic-field model derived in [10] from the field's divergence-free and curl-free properties to establish the relationship between the platform's position and orientation changes and the model. For enhanced robustness, we employ a stochastic clone EKF (SC-EKF) to fuse magnetometer-array measurements with inertial data. In addition, the algorithm incorporates a magnetic-vector constraint to address the unobservability of absolute heading.

The remainder of this article is structured as follows. Section II derives the local magnetic-field model. Section III details the filtering algorithm for data fusion. Section IV analyzes algorithm performance using both public and proprietary datasets, and examines the impact of varying magnetic gradient intensities. Finally, Section V concludes this article and proposes directions for future work.

II. Magnetic-Field Related Model Construction

Given that this article involves numerous coordinate transformations, the primary variables and coordinate systems are summarized in Nomenclature for clarity.

A. Local Magnetic-Field Modeling

Local magnetic-field modeling refers to the mathematical fitting and parameterization of the magnetic-field distribution within a bounded spatial region. Under the assumptions that there are no free electric charges in the space and that external magnetic interference sources are sufficiently distant, the local magnetic-field model satisfies the physical conditions of being both curl-free and divergence-free. Letting $\boldsymbol{M}(\boldsymbol{r},\boldsymbol{\mu})$ denote the local magnetic-field model, the following conditions hold [10]:

$$\nabla_{\boldsymbol{r}} \times \boldsymbol{M}(\boldsymbol{r},\boldsymbol{\mu}) = 0 \tag{1}$$

$$\nabla_{\boldsymbol{r}} \cdot \boldsymbol{M}(\boldsymbol{r},\boldsymbol{\mu}) = 0. \tag{2}$$

Here, $\boldsymbol{r} = [x, y, z]^\top$ denotes the position vector from the origin of the local magnetic-field model to an arbitrary point in space. The vector $\boldsymbol{\mu}$ represents the coefficients of the magnetic-field polynomial model, with its dimensionality determined by the order l of the polynomial. Huang et al. [10], a scalar magnetic potential function was introduced and expanded as an lth order polynomial at position $\boldsymbol{r}$. By eliminating redundant parameters, an explicit linear parametric model for the magnetic field is ultimately obtained

$$\boldsymbol{M}(\boldsymbol{r},\boldsymbol{\theta}) = \boldsymbol{\Phi}(\boldsymbol{r})\boldsymbol{\theta}. \tag{3}$$

Here, $\boldsymbol{\theta}$ represents the coefficient vector of the local magnetic-field model, and its dimension is determined by the model order l, i.e., $\dim(\boldsymbol{\theta}) = l^2 + 4l + 3$. The matrix $\boldsymbol{\Phi}(\boldsymbol{r})$ denotes the coefficient matrix constructed from spatial terms. For example, in the case of a first-order magnetic-field model, $\boldsymbol{\Phi}(\boldsymbol{r})$ can be expressed as

$$\boldsymbol{\Phi}(\boldsymbol{r}) = \begin{bmatrix} 1 & 0 & 0 & y & z & 0 & 2x & 0 \\ 0 & 1 & 0 & x & 0 & z & 0 & 2y \\ 0 & 0 & 1 & 0 & x & y & -2z & -2z \end{bmatrix}. \tag{4}$$

The local magnetic-field model equation shown in (3) applies to any coordinate system.

B. Magnetic-Field–Pose Relationship Modeling

To establish the relationship between magnetic-field variation and relative pose change, it is essential to examine the relationship between magnetic-field vectors measured at the same spatial location across two consecutive time steps. The magnetic-field vectors in the body frame (b-frame) at two consecutive time instants satisfy the following relationship:

$$\boldsymbol{M}^{b_j}\left(\boldsymbol{l}^{b_j},\boldsymbol{\theta}_j\right) = \boldsymbol{C}_{b_i}^{b_j}\boldsymbol{M}^{b_i}\left(\boldsymbol{l}^{b_i},\boldsymbol{\theta}_i\right) \tag{5}$$

$$\boldsymbol{\Phi}\left(\boldsymbol{l}^{b_j}\right)\boldsymbol{\theta}_j = \boldsymbol{C}_{b_i}^{b_j}\boldsymbol{\Phi}\left(\boldsymbol{l}^{b_i}\right)\boldsymbol{\theta}_i \tag{6}$$

$$\boldsymbol{l}^{b_i} = \begin{bmatrix} \boldsymbol{r}_1 & \boldsymbol{r}_2 & \boldsymbol{r}_3 & \boldsymbol{r}_4 & \boldsymbol{r}_5 \end{bmatrix}^\top \tag{7}$$

where b_i and b_j denote the body frame at the current and previous time instants, respectively. Fig. 1 illustrates the geometric relationship between the body frames (b_i and b_j) at two consecutive time instants. $\boldsymbol{l}^{b_i}$ denotes the coordinates of magnetometers in the b_i-frame. These coordinates are defined as the positions of each magnetometer relative to the origin of a chosen body frame. Since the magnetometers are rigidly mounted with respect to each other, their coordinates remain constant in the b_i-frame. The complete construction of $\boldsymbol{\Phi}(\boldsymbol{l}^{b_i})$ is defined as follows:

$$\boldsymbol{\Phi}\left(\boldsymbol{l}^{b_i}\right) = \begin{bmatrix} \boldsymbol{\Phi}(\boldsymbol{r}_1) \\ \boldsymbol{\Phi}(\boldsymbol{r}_2) \\ \boldsymbol{\Phi}(\boldsymbol{r}_3) \\ \boldsymbol{\Phi}(\boldsymbol{r}_4) \\ \boldsymbol{\Phi}(\boldsymbol{r}_5) \end{bmatrix}. \tag{8}$$

The parameters $\hat{\boldsymbol{\theta}}$ of the magnetic-field model can be estimated via least squares using observations from the magnetometer array and (3)

$$\hat{\boldsymbol{\theta}} = \left(\boldsymbol{\Phi}^\top\left(\boldsymbol{l}_i^{b_i}\right)\boldsymbol{\Phi}\left(\boldsymbol{l}_i^{b_i}\right)\right)^{-1}\boldsymbol{\Phi}\left(\boldsymbol{l}_i^{b_i}\right)^\top\boldsymbol{M}^{b_i}. \tag{9}$$

Here $\boldsymbol{M}^{b_i}$ represents the observation vector of magnetometer array, and $\boldsymbol{\Phi}(\boldsymbol{l}_i^{b_i})$ is the coefficient matrix constructed from the coordinate vector $\boldsymbol{l}_i^{b_i}$ following (4) and (8). From the construction of the matrix $\boldsymbol{\Phi}$, it can be seen that a necessary condition for $\boldsymbol{\Phi}^\top(\boldsymbol{l}_i^{b_i})\boldsymbol{\Phi}(\boldsymbol{l}_i^{b_i})$ to be invertible is having at least three coordinates $\boldsymbol{r}_i$, such that the nine scalar equations generated by these coordinates render the eight columns of $\boldsymbol{\Phi}$ linearly independent. In this work, this condition is ensured by appropriately arranging the geometric configuration of the magnetometer array. The estimation covariance matrix for the local magnetic-field model parameters $\hat{\boldsymbol{\theta}}$ is

$$\boldsymbol{Cov}_{\hat{\boldsymbol{\theta}}} = \sigma^2\left(\boldsymbol{\Phi}^\top\boldsymbol{\Phi}\right)^{-1} \tag{10}$$

where σ^2 is estimated by calculating the sum of squares of model residuals.

Subsequently, the local magnetic-field parameters $\hat{\boldsymbol{\theta}}$ are utilized to predict the magnetic-field observation $\hat{\boldsymbol{M}}_j^{b_i}$ at the previous time step. We assume that the parameters of the magnetic-field model do not change significantly between two adjacent moments

$$\hat{\boldsymbol{M}}_j^{b_i} = \boldsymbol{\Phi}\left(\boldsymbol{l}_j^{b_i}\right)\hat{\boldsymbol{\theta}} \tag{11}$$

where $\boldsymbol{l}_j^{b_i}$ denotes the coordinates of magnetometers in the b_i-frame at the previous time. Since the magnetometers are rigidly mounted on the platform assembly, the coordinate relationship $\boldsymbol{l}_j^{b_j} = \boldsymbol{l}_i^{b_i}$. The relative motion of the platform between two time instances, including both translational and rotational components, can be formulated as follows:

$$\boldsymbol{l}_j^{b_i} = \boldsymbol{C}_j^i\boldsymbol{l}_j^{b_j} + \Delta\boldsymbol{r}^{b_i} \tag{12}$$

$$\boldsymbol{C}_j^i = \boldsymbol{C}_n^{b_i}\boldsymbol{C}_{b_j}^n \tag{13}$$

$$\Delta\boldsymbol{r}^{b_i} = \boldsymbol{C}_n^{b_i}\Delta\boldsymbol{r}_i^n = \boldsymbol{C}_n^{b_i}\left(\boldsymbol{r}_j^n - \boldsymbol{r}_i^n\right) \tag{14}$$

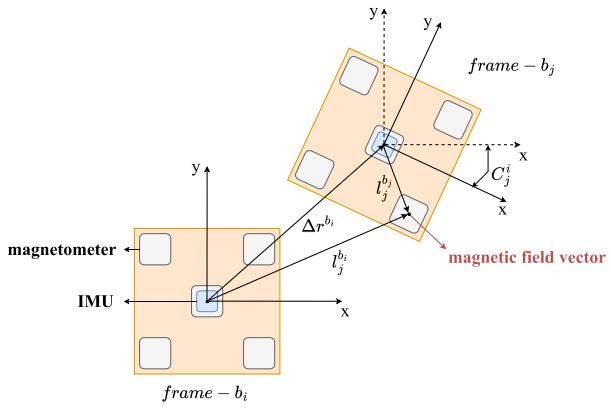

Fig. 1. 2-D illustration of the geometric relationship between the body frames at two consecutive times.

where $\boldsymbol{C}_j^i$ represents the relative rotation between the b_i-frame and b_j-frame at consecutive time steps, $\Delta \boldsymbol{r}^{b_i}$ denotes the position variation in the b-frame. Synthesizing (5), (6), and (11)~(14) yields the predicted magnetic-field value $\hat{\boldsymbol{M}}_j^{b_j}$ from the previous time step

$$\hat{\boldsymbol{M}}_j^{b_j} = \boldsymbol{C}_i^j \boldsymbol{\Phi}\left(\boldsymbol{C}_j^i \boldsymbol{l}_j^{b_j} + \boldsymbol{C}_n^{b_i}\left(\boldsymbol{r}_j^n - \boldsymbol{r}_i^n\right)\right)\hat{\boldsymbol{\theta}}. \tag{15}$$

Equation (15) encodes the principle that, within a sufficiently small spatiotemporal neighborhood, the local magnetic-field parameters $\boldsymbol{\theta}$ remain constant. Within the model's effective domain, we attribute observed magnetic fluctuations to changes in the platform's pose. By collecting magnetic-field observations within this domain, we then employ perturbation analysis to derive relationships between variations in the magnetic gradient and changes in the platform's pose. These relationships yield constraint terms derived from observations, which we integrate into the filtering framework to improve state-estimation accuracy.

III. Magnetometer Array Constraint Based on SC-EKF

The data fusion algorithm proposed in this article is based on the concept of inertial mechanization combined with pose correction using a magnetic-field model. While the INS mechanization propagates the navigation solution, discrepancies between magnetometer-array measurements and magnetic-field model predictions are used to generate pose constraints. To correctly fuse the high-frequency propagation information from INS with the relative pose measurements observed by the magnetometer array, a SC-EKF is employed as the filtering framework.

This section presents an overview of the proposed data fusion algorithm. Fig. 2 presents the algorithm's flowchart. First, strap-down inertial navigation mechanization is executed to determine the carrier's current position, velocity, and attitude. Next, magnetic array measurements are used to estimate the parameters of the local magnetic-field model. Subsequently, historical state information is employed to compute relative pose changes between successive epochs and to predict the corresponding magnetic-field models. These predictions

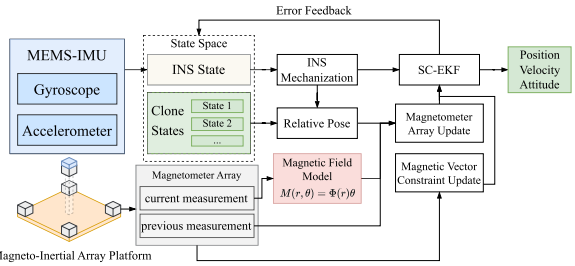

Fig. 2. Algorithm flowchart of SC-EKF-MIO.

are then combined with magnetic array measurements from adjacent epochs to formulate updated constraints. Finally, the SC-EKF is applied to fuse magnetic-field model variations with the propagated states from inertial integration. In Addition, the algorithm incorporates magnetic-vector constraints in the navigation frame to improve heading angle estimation.

A. Inertial Navigation Algorithm

The INS Mechanization algorithm is based on the idea that the current position, velocity, and attitude of a moving object can be obtained by integrating acceleration twice and angular rate once, given the initial navigation state. In this article, a low-cost MEMS-IMU is employed for mechanization, allowing minor corrections (e.g., Earth rotation effects) to be neglected. The simplified mechanization in the navigation frame (n-frame) is expressed as follows [23]:

$$\begin{bmatrix} \boldsymbol{r}_k^n \\ \boldsymbol{v}_k^n \\ \boldsymbol{C}_{b,k}^n \end{bmatrix} = \begin{bmatrix} \boldsymbol{r}_{k-1}^n + \boldsymbol{v}_k^n \Delta t \\ \boldsymbol{v}_{k-1}^n + \left[\boldsymbol{C}_{b,k}^n\left(\tilde{\boldsymbol{f}}_k^b - \boldsymbol{b}_a\right) + \boldsymbol{g}^n\right]\Delta t \\ \boldsymbol{C}_{b,k-1}^n + \boldsymbol{C}_{b,k-1}^n\left[\left(\tilde{\boldsymbol{\omega}}_k^b - \boldsymbol{b}_g\right)\times\right]\Delta t \end{bmatrix} \tag{16}$$

where $\boldsymbol{r}^n$ and $\boldsymbol{v}^n$ represent the position vector and the velocity vector in the n-frame respectively, $\boldsymbol{C}_b^n$ represents the transformation matrix from the b-frame to the n-frame, $\boldsymbol{g}^n$ represents the Earth gravity vector in the n-frame, $\tilde{\boldsymbol{f}}_k^b$ and $\tilde{\boldsymbol{\omega}}_k^b$ represent the acceleration measurement vector and angle rate measurement in the b-frame, respectively. $\boldsymbol{b}_a$ and $\boldsymbol{b}_g$ represent the bias of the accelerometer and gyroscope, respectively. $\Delta t = t_k - t_{k-1}$ represents the time interval between the kth and $(k-1)$th epoch.

B. Stochastic Clone EKF

In the proposed method, an SC-EKF is employed to fuse relative pose change observations provided by the magnetometer array, thereby reducing the accumulation of errors in the INS. Meanwhile, the incremental variation of the magnetic-field vector is used to enhance the estimation of the heading angle, which further improves the accuracy of position estimation.

SC-EKF is principally intended to remedy the classical Kalman filter's inability to properly handle the cross-covariances that arise between the current state and previous states. When an observation depends on both previous and current states, retaining "clones" of previous states in the filter state vector and explicitly computing the associated cross terms is beneficial. This allows relative measurements to be incorporated into the Kalman update in an optimal way under

first-order linearization. This leads to more consistent and more accurate estimates [24]. The measurements employed by the proposed algorithm intrinsically represent relative pose changes inferred from gradients of the local magnetic field; they are therefore relative observations with temporal correlation. Adopting SC-EKF enables more effective use of these observations while accurately estimating the system state.

To fuse both magnetometer observations and magnetic-field measurements in the navigation frame, the proposed method incorporates the concept of stochastic cloning into the error-state Kalman filter (ESKF) framework, resulting in an indirect SC-EKF approach. At time k, the $(15 + 3 \times m)$-dimensional error-state variables are defined as

$$\delta \boldsymbol{x}_k = \begin{bmatrix} \boldsymbol{s}_k & \boldsymbol{\eta}_k \end{bmatrix}^\top \tag{17}$$

where

$$\boldsymbol{\eta}_k = \begin{bmatrix} \delta \boldsymbol{r}^n_{k-m} & \delta \boldsymbol{r}^n_{k-m+1} & \cdots & \delta \boldsymbol{r}^n_{k-1} \end{bmatrix}^\top \tag{18}$$

$$\boldsymbol{s}_k = \begin{bmatrix} \delta \boldsymbol{r}^n_k & \delta \boldsymbol{v}^n_k & \boldsymbol{\phi}_k & \delta \boldsymbol{b}_{g,k} & \delta \boldsymbol{b}_{a,k} \end{bmatrix}^\top \tag{19}$$

where $\delta \boldsymbol{r}^n$, $\delta \boldsymbol{v}^n$, and $\boldsymbol{\phi}$ represent the error vectors of position, velocity, and attitude in the n-frame, respectively. $\delta \boldsymbol{b}_g$ and $\delta \boldsymbol{b}_a$ represent the error vectors for gyroscope and accelerometer biases, respectively. k denotes the epoch index, m specifies the number of historical states retained in the sliding window, and $\delta \boldsymbol{r}^n_{k-m}$ and $\delta \boldsymbol{r}^n_{k-1}$ represent the position error vectors of the historical states. The discretized and linearized system error model can be formulated as follows:

$$\begin{cases} \delta \boldsymbol{x}_{k|k-1} = \boldsymbol{\Phi}_{k-1} \delta \boldsymbol{x}_{k-1|k-1} + \boldsymbol{w}_k \\ \delta \boldsymbol{z}_k = \boldsymbol{H}_k \delta \boldsymbol{x}_{k|k-1} + \boldsymbol{n}_k \end{cases} \tag{20}$$

where the subscripts $k-1$ and k represent the epoch, $\delta \boldsymbol{x}_{k-1|k-1}$ and $\delta \boldsymbol{x}_{k|k-1}$ represent the previous and predicted error-state vectors, respectively. $\delta \boldsymbol{z}_k$ represents the measurement misclosure vector, $\boldsymbol{H}_k$ is the observation matrix, $\boldsymbol{w}_k$ and $\boldsymbol{n}_k$ are the process noise and measurement noise, respectively. The state transition matrix $\boldsymbol{\Phi}_k$ is expressed as follows:

$$\boldsymbol{\Phi}_{k,15\times 15} = \begin{bmatrix} \boldsymbol{I}_3 & \boldsymbol{I}_3 \Delta t & \boldsymbol{0}_3 & \boldsymbol{0}_3 & \boldsymbol{0}_3 \\ \boldsymbol{0}_3 & \boldsymbol{I}_3 & \left(\boldsymbol{f}^n_k \times\right) \Delta t & \boldsymbol{0}_3 & \boldsymbol{C}^n_{b,k} \Delta t \\ \boldsymbol{0}_3 & \boldsymbol{0}_3 & \boldsymbol{I}_3 & -\boldsymbol{C}^n_{b,k} \Delta t & \boldsymbol{0}_3 \\ \boldsymbol{0}_3 & \boldsymbol{0}_3 & \boldsymbol{0}_3 & \boldsymbol{I}_3 & \boldsymbol{0}_3 \\ \boldsymbol{0}_3 & \boldsymbol{0}_3 & \boldsymbol{0}_3 & \boldsymbol{0}_3 & \boldsymbol{I}_3 \end{bmatrix} \tag{21}$$

$$\boldsymbol{\Phi}_k = \begin{bmatrix} \boldsymbol{\Phi}_{k,15\times 15} & \boldsymbol{0}_{15\times 3m} \\ \boldsymbol{0}_{3m\times 15} & \boldsymbol{I}_{3m\times 3m} \end{bmatrix}. \tag{22}$$

In the SC-EKF framework, cloned states(augmented historical states) do not require updates during the propagation phase. After state propagation, the covariance propagation formula is expressed as

$$\boldsymbol{P}_{k,k-1} = \boldsymbol{\Phi}_{k-1} \boldsymbol{P}_{k-1} \boldsymbol{\Phi}^\top_{k-1} + \boldsymbol{Q}_k \tag{23}$$

where $\boldsymbol{P}_{k-1}$ denotes the initial state covariance matrix, $\boldsymbol{Q}_k$ denotes the process noise covariance matrix for state prediction.

When valid observations are acquired, the following formula can be applied to update the state vector and its associated covariance matrix:

$$\delta \boldsymbol{x}_k = \delta \boldsymbol{x}_{k,k-1} + \boldsymbol{K}_k \left(\delta \boldsymbol{z}_k - \boldsymbol{H}_k \boldsymbol{x}_{k,k-1}\right) \tag{24}$$

$$\boldsymbol{P}_k = (\boldsymbol{I} - \boldsymbol{K}_k \boldsymbol{H}_k) \boldsymbol{P}_{k,k-1} (\boldsymbol{I} - \boldsymbol{K}_k \boldsymbol{H}_k)^\top + \boldsymbol{K}_k \boldsymbol{R}_k \boldsymbol{K}^\top_k \tag{25}$$

$$\boldsymbol{K}_k = \boldsymbol{P}_{k,k-1} \boldsymbol{H}^\top_k \left(\boldsymbol{H}_k \boldsymbol{P}_{k,k-1} \boldsymbol{H}^\top_k + \boldsymbol{R}_k\right)^{-1}. \tag{26}$$

It is noteworthy that after the SC-EKF completes the state vector update, a block permutation of the current covariance matrix $\boldsymbol{P}_k$ must be performed. This step aims to manage the m historical cloned states in the sliding window and ensure structural consistency between the covariance matrix and the state vector. The probability propagation of the stochastic clone step in the proposed system is defined as

$$\boldsymbol{P}^{\text{new}}_k = \begin{bmatrix} \boldsymbol{I}_{15} & \boldsymbol{0}_{15\times(3m)} \\ \boldsymbol{A} \end{bmatrix} \boldsymbol{P}_k \begin{bmatrix} \boldsymbol{I}_{15} & \boldsymbol{0}_{15\times(3m)} \\ \boldsymbol{A} \end{bmatrix}^\top \tag{27}$$

$$\boldsymbol{A} = \begin{bmatrix} \boldsymbol{0}_{3(m-1)\times 3} & \boldsymbol{0}_{3(m-1)\times 15} & \boldsymbol{I}_{3(m-1)\times 3(m-1)} \\ \boldsymbol{I}_3 & \boldsymbol{0}_{3\times 15} & \boldsymbol{0}_{3\times 3(m-1)} \end{bmatrix} \tag{28}$$

where the rows and columns of $\boldsymbol{A}$ are $(3m)$ and $(15 + 3m)$.

To better illustrate the mechanism of stochastic cloning adopted in this study, Fig. 3 presents a schematic of the sliding-window update process. The sliding window maintains m historical states, each storing the corresponding position. Simultaneously, the position error is augmented into the error-state vector, as shown in (17) and (18). After the filtering update at time step k, the current navigation state is compensated, and the positions are cloned as a new state. This newly cloned state is then inserted into the sliding window, while the oldest (i.e., the mth) clone is marginalized. During the compensation phase, all stored positions within the sliding window are also updated to maintain consistency in the state estimation.

C. Magnetometer Array Constraint Update

In Section II-B, we have established the relationship between the local magnetic-field model and the platform's position and orientation changes, as shown in (15). The next step is to perform perturbation analysis in order to further derive the relationship between the magnetic-field model and the error-state variables of interest. Perturbation analysis of the (15) can be expressed as follows:

$$\begin{aligned} \hat{\boldsymbol{M}}^{b_j}_j &= \hat{\boldsymbol{C}}^j_i \hat{\boldsymbol{\Phi}} \left(\boldsymbol{l}^{b_i}_j\right) \boldsymbol{\theta} \\ &= \left(\boldsymbol{C}^j_i + \left[\left(\delta \boldsymbol{b}_g dt + \boldsymbol{\eta}_\omega\right) \times\right]\right) \left(\boldsymbol{\Phi}\left(\boldsymbol{l}^{b_i}_j\right) \boldsymbol{\theta} + \boldsymbol{B}(\boldsymbol{\theta}) \delta \boldsymbol{l}^{b_i}_j\right) \\ &\approx \boldsymbol{C}^j_i \boldsymbol{\Phi}\left(\boldsymbol{l}^{b_i}_j\right) \boldsymbol{\theta} + \boldsymbol{C}^j_i \boldsymbol{B}(\boldsymbol{\theta}) \delta \boldsymbol{l}^{b_i}_j + \left[\left(\delta \boldsymbol{b}_g dt + \boldsymbol{\eta}_\omega\right) \times\right] \boldsymbol{\Phi}\left(\boldsymbol{l}^{b_i}_j\right) \boldsymbol{\theta} \\ &= \boldsymbol{M}^{b_j}_j + \boldsymbol{C}^j_i \boldsymbol{B}(\boldsymbol{\theta}) \delta \boldsymbol{l}^{b_i}_j - \left[\boldsymbol{M}^{b_i}_j \times\right] \delta \boldsymbol{b}_g dt - \left[\boldsymbol{M}^{b_i}_j \times\right] \boldsymbol{\eta}_\omega \end{aligned} \tag{29}$$

where dt denotes the time interval between two consecutive magnetometer array update steps. The parameter $\boldsymbol{\theta}$ in the equation is estimated using the least-squares method based on the measurements from all magnetometers at the time step i, as described in (9). $\boldsymbol{\eta}_\omega \sim \mathcal{N}(\boldsymbol{0}, \boldsymbol{q}_\omega dt \boldsymbol{I}_3)$, denotes the angular error noise vector generated by integrating the gyroscope measurement noise. Since the gyroscope measurement noise does not alter the structure of the Jacobian matrix in the observation equation but rather appears as an additional observation noise term, this component is omitted in the subsequent derivation of the relative attitude. It is explicitly included in the final

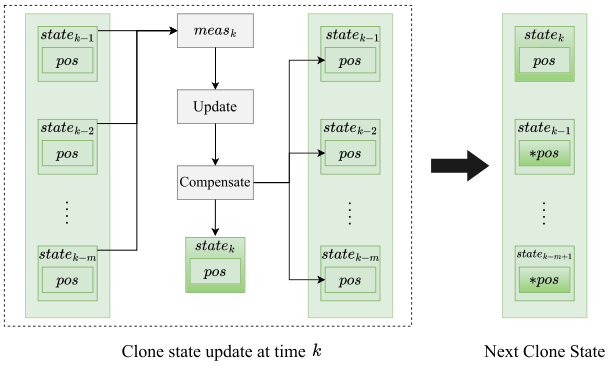

Fig. 3. Illustration of sliding-window update for stochastic cloning.

observation noise matrix. Taking the first-order magnetic-field model as an example, $\boldsymbol{B}(\boldsymbol{\theta})$ is formulated as

$$\boldsymbol{B}(\boldsymbol{\theta}) = \begin{bmatrix} 2\theta_4 & \theta_6 & \theta_7 \\ \theta_6 & 2\theta_5 & \theta_8 \\ \theta_7 & \theta_8 & -2(\theta_4+\theta_5) \end{bmatrix}. \tag{30}$$

Perturbation analysis of $\boldsymbol{l}_j^{b_i}$ can be expressed as follows:

$$\begin{aligned} \hat{\boldsymbol{l}}_j^{b_i} &= \hat{\boldsymbol{C}}_j^i \hat{\boldsymbol{l}}_j^{b_j} + \hat{\boldsymbol{C}}_n^{b_i} \Delta\hat{\boldsymbol{r}}^n \\ &= \left(\boldsymbol{C}_j^i - \left[\delta\boldsymbol{b}_g dt\times\right]\right)\boldsymbol{l}_j^{b_j} + \left[\boldsymbol{I} - \boldsymbol{\phi}\times\right]\boldsymbol{C}_n^{b_i}\left(\hat{\boldsymbol{r}}_j^n - \hat{\boldsymbol{r}}_i^n\right) \\ &= \boldsymbol{l}_j^{b_i} + \boldsymbol{C}_n^{b_i}\delta\boldsymbol{r}_j^n - \boldsymbol{C}_n^{b_i}\delta\boldsymbol{r}_i^n + \left[\boldsymbol{l}_j^{b_j}\times\right]\delta\boldsymbol{b}_g dt + \left[\Delta\boldsymbol{r}^{b_i}\times\right]\boldsymbol{\phi} \\ \delta\boldsymbol{l}_j^{b_i} &= \boldsymbol{C}_n^{b_i}\delta\boldsymbol{r}_j^n - \boldsymbol{C}_n^{b_i}\delta\boldsymbol{r}_i^n + \left[\boldsymbol{l}_j^{b_j}\times\right]\delta\boldsymbol{b}_g dt + \left[\Delta\boldsymbol{r}^{b_i}\times\right]\boldsymbol{\phi}. \end{aligned} \tag{31}$$

By combining the above two equations, the error perturbation equation of the magnetic-field model with respect to the error-state variables can be obtained

$$\begin{aligned} \hat{\boldsymbol{M}}_j^{b_j} &= \boldsymbol{M}_j^{b_j} + \boldsymbol{C}_i^j\boldsymbol{B}(\boldsymbol{\theta})\delta\boldsymbol{l}_j^{b_i} - \left[\boldsymbol{M}_j^{b_i}\times\right]\delta\boldsymbol{b}_g dt \\ &= \boldsymbol{M}_j^{b_j} + \boldsymbol{C}_i^j\boldsymbol{B}(\boldsymbol{\theta})\boldsymbol{C}_n^{b_i}\delta\boldsymbol{r}_j^n - \boldsymbol{C}_i^j\boldsymbol{B}(\boldsymbol{\theta})\boldsymbol{C}_n^{b_i}\delta\boldsymbol{r}_i^n \\ &\quad + \left(\boldsymbol{C}_i^j\boldsymbol{B}(\boldsymbol{\theta})\left[\boldsymbol{l}_j^{b_j}\times\right] - \left[\boldsymbol{M}_j^{b_i}\times\right]\right)\delta\boldsymbol{b}_g dt \\ &\quad + \boldsymbol{C}_i^j\boldsymbol{B}(\boldsymbol{\theta})\left[\Delta\boldsymbol{r}^{b_i}\times\right]\boldsymbol{\phi}. \end{aligned} \tag{32}$$

For the magnetic field from the previous epoch, the corresponding observations can be obtained via magnetometer array measurements as follows:

$$\tilde{\boldsymbol{M}}_j^{b_j} = \boldsymbol{M}_j^{b_j} + \boldsymbol{n}_v \tag{33}$$

where $\boldsymbol{n}_v$ denotes the observation noise. By combining (32) and (33), the measurement model in the error-state Kalman filter framework can be expressed as

$$\begin{aligned} \delta\boldsymbol{z}_{\mathrm{MA}} &= \hat{\boldsymbol{M}}_j^{b_j} - \tilde{\boldsymbol{M}}_j^{b_j} \\ &= \boldsymbol{C}_i^j\boldsymbol{B}(\boldsymbol{\theta})\boldsymbol{C}_n^{b_i}\delta\boldsymbol{r}_j^n - \boldsymbol{C}_i^j\boldsymbol{B}(\boldsymbol{\theta})\boldsymbol{C}_n^{b_i}\delta\boldsymbol{r}_i^n \\ &\quad + \left(\boldsymbol{C}_i^j\boldsymbol{B}(\boldsymbol{\theta})\left[\boldsymbol{l}_j^{b_j}\times\right] - \left[\boldsymbol{M}_j^{b_i}\times\right]\right)\delta\boldsymbol{b}_g dt \\ &\quad + \boldsymbol{C}_i^j\boldsymbol{B}(\boldsymbol{\theta})\left[\Delta\boldsymbol{r}^{b_i}\times\right]\boldsymbol{\phi} + \boldsymbol{n}_v. \end{aligned} \tag{34}$$

As derived in Section II, the observation equation (34) utilizing magnetometer array measurements for the filter's measurement update has been established. Therefore, the design matrix can be formulated as

$$\boldsymbol{H}_{\mathrm{mag}} = \begin{bmatrix} -\boldsymbol{H}_{11} & \boldsymbol{0}_3 & \boldsymbol{H}_{13} & \boldsymbol{H}_{14} & \boldsymbol{0}_3 & \boldsymbol{0}_3 & \cdots & \boldsymbol{H}_{11} \end{bmatrix}. \tag{35}$$

The submatrix in $\boldsymbol{H}_{\mathrm{mag}}$ is defined as

$$\begin{cases} \boldsymbol{H}_{11} = \boldsymbol{C}_i^j\boldsymbol{B}(\boldsymbol{\theta})\boldsymbol{C}_n^{b_i} \\ \boldsymbol{H}_{13} = \boldsymbol{C}_i^j\boldsymbol{B}(\boldsymbol{\theta})\left[\Delta\boldsymbol{r}^{b_i}\times\right] \\ \boldsymbol{H}_{14} = \left(\boldsymbol{C}_i^j\boldsymbol{B}(\boldsymbol{\theta})\left[\boldsymbol{l}_j^{b_j}\times\right] - \left[\boldsymbol{M}_j^{b_i}\times\right]\right)dt. \end{cases} \tag{36}$$

Since $\delta\boldsymbol{z}_{\mathrm{mag}}$ contains the measurement noise and estimation error of the magnetic-field model parameters, as well as the gyroscope measurement noise, the observation covariance matrix should therefore consist of the following components:

$$\begin{aligned} \boldsymbol{R}_{\mathrm{meas}} &= \left(\boldsymbol{C}_i^j\boldsymbol{\Phi}\left(\boldsymbol{l}_j^{b_i}\right)\right)\boldsymbol{Cov}_{\hat{\theta}}\left(\boldsymbol{C}_i^j\boldsymbol{\Phi}\left(\boldsymbol{l}_j^{b_i}\right)\right)^{\top} \\ &\quad + \mathrm{diag}\left(\sigma_{\mathrm{mag}}^2\right) + \left[\boldsymbol{M}_j^{b_i}\times\right]\left(\boldsymbol{q}_\omega dt\boldsymbol{I}_3\right)\left[\boldsymbol{M}_j^{b_i}\times\right]^{\top}. \end{aligned} \tag{37}$$

Here σ_{mag}^2 denotes the standard deviation of the magnetometer array measurement noise.

D. Magnetic-Vector Constraint Update

Previous studies [25] have shown a mismatch between estimated state covariance and actual system uncertainty in EKF-based odometry-aided INS implementations. Likewise, in magnetometer array–aided INS scenarios, the heading angle becomes unobservable due to the absence of absolute heading References. However, the EKF's Jacobian linearization introduces higher-order truncation errors, resulting in spurious observability of inherently unobservable states within the covariance matrix. This effect artificially inflates the filter's confidence in heading error estimates, potentially causing filter divergence.

To address heading unobservability, we introduce a magnetic-vector constraint in the navigation frame. This constraint update constructs the measurement by utilizing the difference of the magnetic-field vectors in the navigation frame between adjacent time instants.

Magnetometers are capable of measuring the magnetic-field intensity along the sensor's X-, Y-, and Z-axes. In low-cost magnetometer applications, the effects of scale factor and nonorthogonality errors are generally considered secondary compared to bias and random noise. Therefore, the magnetometer measurement can be modeled as follows [26]:

$$\tilde{\boldsymbol{M}}^b = \boldsymbol{C}_n^b\left(\boldsymbol{M}_G^n + \boldsymbol{M}_I^n\right) + \boldsymbol{b}_m + \boldsymbol{n}_m \tag{38}$$

where $\boldsymbol{M}_G^n$ and $\boldsymbol{M}_I^n$ are the geomagnetic-field and magnetic-field interference in the n-frame, respectively. $\tilde{\boldsymbol{M}}^b$ and $\boldsymbol{b}_m$ are the measurement and bias of magnetometer, respectively. $\boldsymbol{C}_n^b$ is the transformation matrix from the n-frame to the b-frame. $\boldsymbol{n}_m$ is the measurement noise. The geomagnetic field at time k can be expressed as follows:

$$\boldsymbol{M}_{G,k}^n = \boldsymbol{C}_{b,k}^n\left(\tilde{\boldsymbol{M}}_k^b - \boldsymbol{b}_{m,k}\right) + \boldsymbol{M}_{I,k}^n + \boldsymbol{C}_{b,k}^n\boldsymbol{n}_m. \tag{39}$$

Kuang et al. [27] analyzed the magnetic-field vectors observed in typical indoor environments and found that the difference in the magnetic-field vector can significantly reduce the influence of magnetic interference. Based on this observation, it is reasonable to assume that magnetic interference is approximately uniform within a small local area. In other

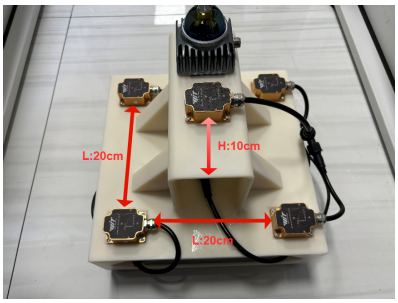

Fig. 4. Sensor array platform.

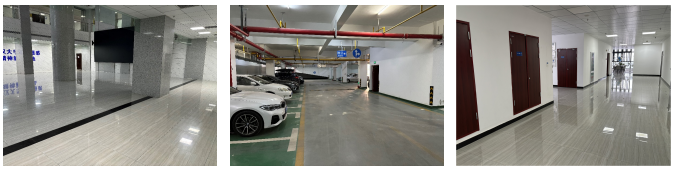

Fig. 5. Data acquisition environment. (a) Scenario a. (b) Scenario b. (c) Scenario c.

words, the magnetic-field vectors at any two time instants within a small region satisfy the following relationship:

$$\mathbf{0} \approx \boldsymbol{M}^n_{G,i} - \boldsymbol{M}^n_{G,j} \tag{40}$$

$$\mathbf{0} \approx \boldsymbol{C}^n_{b,i}\left(\tilde{\boldsymbol{M}}^b_i - \boldsymbol{b}_{m,i}\right) - \boldsymbol{C}^n_{b,j}\left(\tilde{\boldsymbol{M}}^b_j - \boldsymbol{b}_{m,j}\right). \tag{41}$$

Within a short time interval, the magnetometer bias $\boldsymbol{b}_m$ can be regarded as constant. Furthermore, assuming that the attitude and attitude error remain unchanged between adjacent time steps, the above equation simplifies to

$$\mathbf{0} \approx \boldsymbol{C}^n_b\tilde{\boldsymbol{M}}^b_i - \boldsymbol{C}^n_b\tilde{\boldsymbol{M}}^b_j. \tag{42}$$

The perturbation analysis of (42) can be expressed as follows:

$$\begin{aligned}\delta z_{\mathrm{MV}} &= \hat{\boldsymbol{C}}^n_b\tilde{\boldsymbol{M}}^b_i - \hat{\boldsymbol{C}}^n_b\tilde{\boldsymbol{M}}^b_j \\ &= \left[\boldsymbol{I} - \boldsymbol{\phi}\times\right]\boldsymbol{C}^n_b\tilde{\boldsymbol{M}}^b_i - \left[\boldsymbol{I} - \boldsymbol{\phi}\times\right]\boldsymbol{C}^n_b\tilde{\boldsymbol{M}}^b_j \\ &= \tilde{\boldsymbol{M}}^n_i - \tilde{\boldsymbol{M}}^n_j + \left[\left(\tilde{\boldsymbol{M}}^n_i - \tilde{\boldsymbol{M}}^n_j\right)\times\right]\boldsymbol{\phi}\end{aligned} \tag{43}$$

where $\boldsymbol{M}^b_i$ denotes the magnetic-field vector in the body frame at the current epoch; $\boldsymbol{M}^b_j$ denotes the magnetic-field vector in the b-frame at the previous epoch; $\boldsymbol{C}^n_b$ represents the rotation matrix transforming vectors from the b-frame to the navigation frame. The corresponding design matrix is expressed as

$$\boldsymbol{H}_{\mathrm{att}} = \begin{bmatrix}\mathbf{0}_3 & \mathbf{0}_3 & \left[\left(\tilde{\boldsymbol{M}}^n_i - \tilde{\boldsymbol{M}}^n_j\right)\times\right] & \mathbf{0}_3 & \cdots & \mathbf{0}_3\end{bmatrix}. \tag{44}$$

IV. Experimental Results

A. Test Description

To validate the effectiveness of the proposed method, a sensor array platform was constructed, as illustrated in Fig. 4. The platform consists of five HWT-9073 nine-axis sensor modules developed by WitMotion, a Livox Mid-360 LiDAR, and a data logging terminal (not shown in the figure). Each HWT-9073 module integrates a tri-axis accelerometer, a tri-axis gyroscope, and a tri-axis magnetometer. The inertial sensor in each module exhibits a typical bias instability of 60 deg/h and 25 mg, a white noise density of 0.03 deg/ $\sqrt{\mathrm{h}}$ and 0.06 $m/s/\sqrt{\mathrm{h}}$. The magnetometers feature a noise level of 0.1 μT and a resolution of 13 nT.

The sensor configuration shown in Fig. 4 adopts a pyramidal arrangement: four modules are placed at the vertices of a 20 $\times$ 20 cm square, and the fifth module is mounted 10 cm directly above the square's center. The primary reason for selecting this magnetometer array configuration is to enable a more comprehensive perception of the spatial magnetic-field gradient. Based on this consideration, a pyramid-shaped or cross-shaped geometric structure is particularly suitable. [28] provides a detailed analysis of the positioning accuracy achieved with the same number of magnetometers under different geometric configurations, showing that 3-D structures exhibit the most robust performance in 3-D motion scenarios. Furthermore, distributing the magnetometers uniformly in space helps prevent structural degeneracy under extreme conditions, such as collinearity among sensors, which would cause the matrix $\boldsymbol{\Phi}$ to become singular.

Magnetometers are prone to interference from onboard or environmental magnetic disturbances, particularly soft-iron effects, which can cause misalignment between the magnetometer and inertial sensor frames. Therefore, magnetometer calibration and alignment with inertial sensors are necessary before using the magnetometer array for data collection. In the data preprocessing stage of this experiment, a Kalman filter-based magnetometer calibration and alignment algorithm from [26] was applied to ensure measurement accuracy.

The experiments were conducted in three representative indoor environments, as shown in Fig. 5: Scenario a, an office building lobby; Scenario b, an underground parking garage; and Scenario c, an indoor corridor. For the experiments, a pedestrian acted as the carrier of the MIO system. Data acquisition proceeded as follows: the platform was first placed stationary on the floor for a brief initialization period; then the operator held the platform in both hands and walked along a predefined route, ceasing data collection after completing the trajectory segment. During data processing, we evaluated two localization schemes: 1) MAINS: the method proposed in [10] and 2) SC-EKF-MIO: the Livox Mid-360 LiDAR is employed to capture point cloud data during the experiment. It is paired with the Fast-LIO2 [29] algorithm to compute reference trajectories for indoor motion. The relative position error of this LiDAR-inertial fusion system is approximately 0.5% of the total traveled distance. This trajectory serves as the ground truth for evaluating the positioning and orientation accuracy of the proposed method. Time synchronization between the sensors, as well as between the sensors and the reference system, is achieved by simultaneous data acquisition over the serial port. Because all comparisons pertain to relative positioning performance, the initial segment of each test trajectory was aligned with the corresponding portion of the reference trajectory to ensure a fair assessment.

B. Test Results on Dataset

In this section, the ten collected datasets are processed and analyzed. Dataset details are summarized in Table I. Fig. 6 illustrates the horizontal positioning results of both algorithms

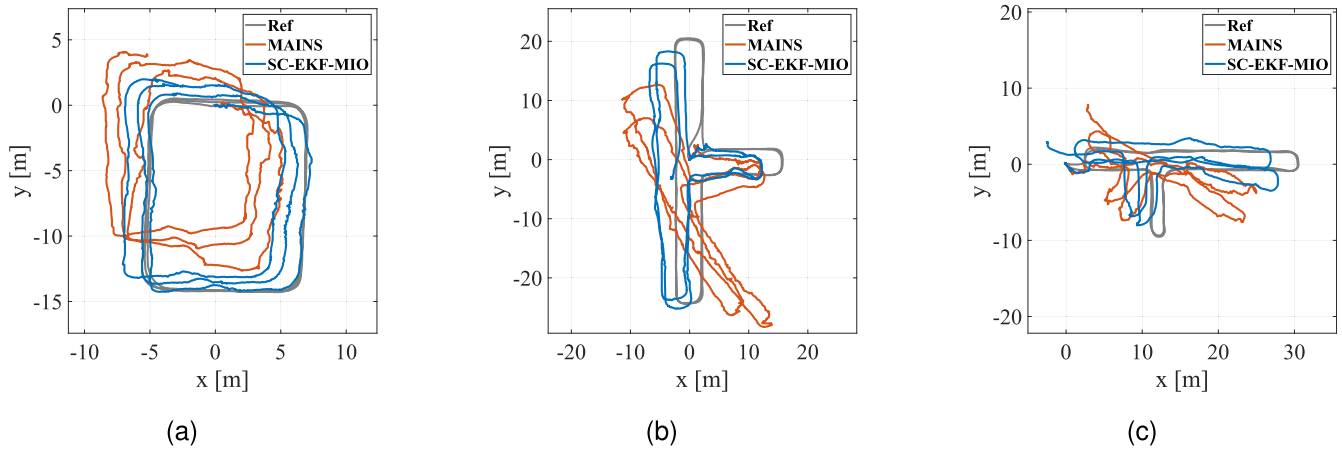

Fig. 6. Trajectory estimation results of our dataset. (a) aM-1. (b) bM-1. (c) cM-1.

TABLE I
INFORMATION ABOUT THE DATASETS

Data sequence	Average height(m)	Length(m)	Duration(s)
aL-1	0.41	146.32	156
aL-2	0.40	143.60	145
aM-1	0.54	149.79	177
aM-2	0.68	148.49	155
aN-1	0.84	137.72	132
aN-2	0.80	138.14	139
bM-1	0.68	247.17	254
bM-2	0.63	248.49	303
cM-1	0.54	155.75	175
cM-2	0.50	154.77	173

L: low height M: medium height N: normal height

TABLE II
HORIZONTAL POSITION AND VELOCITY ERROR STATISTICS OF OUR DATASET

Data sequence	aM-1	aM-2	bM-1	bM-2	cM-1	cM-2
MAINS						
RMS (m)	6.09	9.04	7.61	12.58	4.66	3.11
CDF68 (m)	6.80	9.79	7.99	12.94	4.81	3.39
RMS Speed (m/s)	0.21	0.21	0.19	0.20	0.23	0.24
SC-EKF-MIO						
RMS (m)	1.88	3.13	3.07	2.77	2.58	2.48
CDF68 (m)	2.23	4.00	3.33	3.08	2.98	3.07
RMS Speed (m/s)	0.12	0.15	0.13	0.11	0.13	0.14

across three different experimental scenarios. Table II provides the statistical metrics of positioning results for two datasets per scene in the three scenarios.

The experimental results demonstrate that the proposed SC-EKF-MIO algorithm exhibits significant advantages in horizontal positioning accuracy compared to the MAINS. As shown in Fig. 6, under closed-loop multilap path testing scenarios, the MAINS algorithm displays noticeable trajectory drift, whereas the SC-EKF-MIO maintains close alignment with the reference trajectory. In terms of accuracy metrics, the MAINS method exhibits an average horizontal position error rms exceeding 7 m, whereas the SC-EKF-MIO method achieves an average horizontal position error rms of under 2.5 m. Quantitative comparisons in Table II further validate this conclusion: on datasets with trajectory lengths of 150–250 m, the 68% cumulative distribution function value of horizontal position errors for SC-EKF-MIO averages approximately 2.4 m, representing a reduction of about 60% compared to MAINS's 6.3 m. In terms of speed estimation accuracy, SC-EKF-MIO achieves an average horizontal speed error rms of 0.13 m/s, representing an improvement of approximately 38.1% over MAINS's average of 0.21 m/s.

The pronounced accuracy gains of the proposed algorithm can be attributed to two key factors. First, by leveraging stochastic cloning within a sliding-window framework, the method maintains a sequence of historical states over a fixed time horizon. Each incoming observation simultaneously updates both the current state and the contributions of past states, yielding a smoothing-like effect and making more comprehensive use of the available measurements than the traditional ESKF implementation in MAINS. In addition, the proposed algorithm incorporates magnetic-vector heading correction by leveraging interframe differences in magnetic-field vectors to enhance heading estimation performance. Detailed improvements in heading accuracy will be discussed in Section IV-D.

Fig. 7 shows normalized magnetic-field magnitude maps for three different scenarios. As illustrated, the magnetic-field distributions vary significantly across these typical environments. However, when comparing the corresponding trajectory sets in Fig. 6, it is evident that these differences in magnetic characteristics do not lead to appreciable fluctuations in the localization performance of SC-EKF-MIO. Despite the distinct structural layouts, the SC-EKF-MIO trajectories remain highly coincident with the reference paths in all cases, demonstrating that the algorithm effectively mitigates the impact of spatial magnetic-field variability. This robustness can be attributed to the method's nonparametric treatment of the magnetic field. This reduction in the state's degrees of freedom not only enhances estimation precision but also avoids the need for complex tuning of the magnetic-field model.

C. Test Results on Public Datasets

In this section, we conduct further validation of the proposed algorithm using the open dataset from MAINS [10]. In the

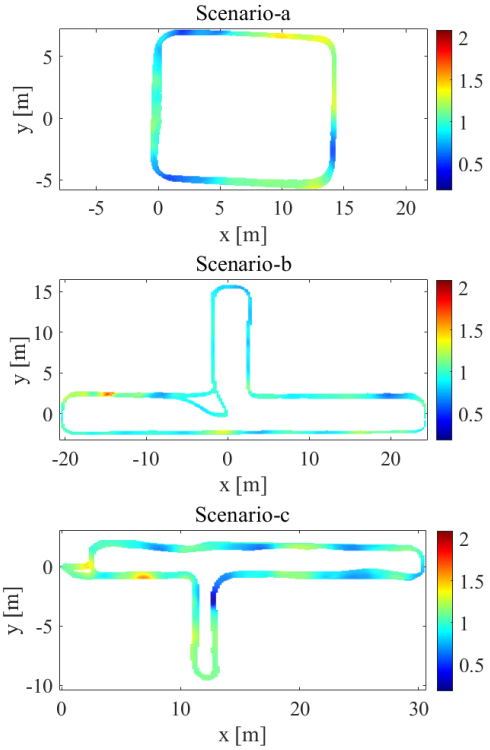

Fig. 7. Magnetic-field magnitude maps in different scenarios.

MAINS experiments, the hardware configuration comprised 30 magnetometers and one MEMS-IMU. For consistency and fairness, our comparison employs the MAINS method with a square array of five magnetometers. In the MAINS study, a motion-capture system provided position measurements for the first 60 s of each test trajectory to aid filter convergence. As no such external assistance exists in practical scenarios, we disable all position-aiding in our comparative evaluation.

Fig. 8 demonstrates the trajectory estimation comparison under a scenario with an average altitude of 0.50 m. The comparison reveals that MAINS exhibits significant cumulative position errors during multiloop motion, accompanied by rapid divergence in heading angle estimates. In contrast, the proposed SC-EKF-MIO algorithm effectively suppresses the accumulation of positional error through its stochastic cloning mechanism and magnetic-vector attitude correction, maintaining tight adherence to the reference trajectory.

According to the statistical results in Table III, the proposed SC-EKF-MIO achieves an rms horizontal position error of approximately 0.56 m on the dataset with an average altitude of 0.50 m, representing an 83% improvement compared to MAINS's 3.44 m. Notably, in velocity estimation, SC-EKF-MIO reduces the rms error by 40% relative to MAINS, demonstrating that the enhanced magnetic-field model and multistate constraints effectively improve the accuracy of velocity estimation. Comparisons of localization results and statistical metrics for the remaining public datasets, along with detailed numerical values, are provided in Table IV and Fig. 9. These results confirm that the proposed

TABLE III

ERROR STATISTICS OF PUBLIC DATASET-1

Data sequence	**LP-1**	**LP-2**	**LP-3**
Trajectory length (m)	114.14	139.87	192.93
Trajectory duration (s)	212	226	332
Average height (m)	0.49	0.52	0.53
MAINS			
RMS (m)	3.15	3.61	3.56
CDF68 (m)	3.36	4.11	3.75
RMS Speed (m/s)	0.09	0.10	0.12
SC-EKF-MIO			
RMS (m)	0.62	0.50	0.58
CDF68 (m)	0.71	0.53	0.61
RMS Speed (m/s)	0.06	0.07	0.08

[1] LP: low height and parallel NP: normal height and parallel NT: normal height and tilted.

TABLE IV

ERROR STATISTICS OF PUBLIC DATASET-2

Data sequence	**NP-1**	**NP-2**	**NP-3**	**NT-1**	**NT-2**
Trajectory length (m)	136.23	132.17	137.76	164.62	137.87
Trajectory duration (s)	177	164	154	185	151
Average height (m)	0.85	0.83	0.79	0.73	0.74
MAINS					
RMS (m)	3.62	2.35	4.21	6.23	3.83
CDF68 (m)	3.77	2.55	4.37	7.25	4.63
RMS Speed (m/s)	0.25	0.19	0.29	0.17	0.14
SC-EKF-MIO					
RMS (m)	3.56	6.68	3.58	3.71	2.87
CDF68 (m)	4.12	7.39	4.11	4.39	3.34
RMS Speed (m/s)	0.17	0.26	0.22	0.10	0.09

[1] LP: low height and parallel NP: normal height and parallel NT: normal height and tilted.

TABLE V

RMS HEADING ANGLE ERROR STATISTICS (UNIT: °)

	aL-1	**aL-2**	**aM-1**	**aM-2**
OFF	3.97	8.90	6.52	19.89
ON	1.82	1.55	1.94	1.90

TABLE VI

RMS VELOCITY ERROR STATISTICS (UNIT: M/S)

	aL-1	**aL-2**	**aM-1**	**aM-2**	**aN-1**	**aN-2**
MAINS	0.27	0.26	0.21	0.21	0.34	0.35
SC-EKF-MIO	0.07	0.08	0.12	0.15	0.18	0.16

SC-EKF-MIO algorithm achieves high-precision localization on open datasets without relying on external positional references.

Fig. 9 shows both algorithms' localization results diverging significantly in position and heading. This behavior arises because the dataset's elevation remains between 0.70 and 0.80 m. We hypothesize that, at this elevation, the magnetic-field gradient attenuates substantially, causing the gradient variations detected by the magnetometer array to flatten. As a result, this flattening introduces errors into the perturbation model linking magnetic gradient variations to pose changes, ultimately causing localization divergence.

D. Analysis of Magnetic-Vector Constraint Update

To validate the optimization effect of the magnetic-vector constraint in the proposed algorithm on attitude estimation,

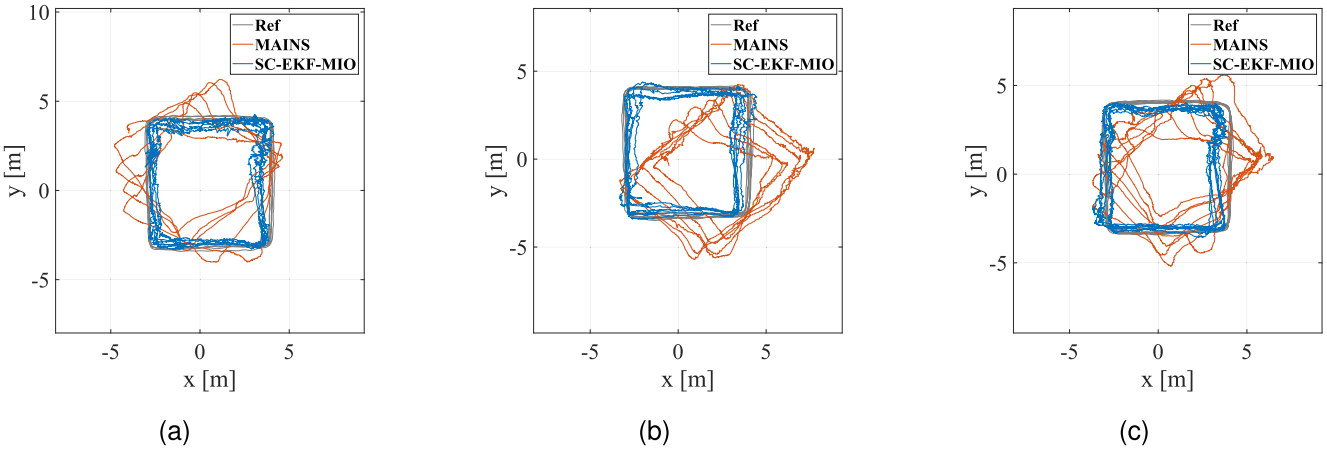

Fig. 8. Trajectory estimation results of public datasets. (a) LP-1. (b) LP-2. (c) LP-3.

TABLE VII
ERROR STATISTICS ON THE PUBLIC DATASET FOR DIFFERENT VALUES OF m

Dataset		Different lengths of the stochastic clone sliding window					
		$m=1$	$m=2$	$m=3$	$m=4$	$m=5$	$m=6$
LP-1	RMS (m)	0.86	**0.62**	0.90	1.21	1.44	1.66
	CDF68 (m)	0.91	**0.71**	0.80	1.07	1.30	1.51
	RMS Speed (m/s)	0.07	**0.06**	0.07	0.08	0.09	0.10
LP-2	RMS (m)	0.98	**0.50**	0.75	1.18	1.50	1.69
	CDF68 (m)	1.03	**0.53**	0.73	1.14	1.46	1.62
	RMS Speed (m/s)	0.09	**0.07**	**0.07**	0.08	0.09	0.10
LP-3	RMS (m)	1.04	**0.58**	0.80	1.30	1.73	2.02
	CDF68 (m)	1.19	**0.61**	0.83	1.39	1.86	2.17
	RMS Speed (m/s)	0.10	**0.08**	**0.08**	0.09	0.10	0.11

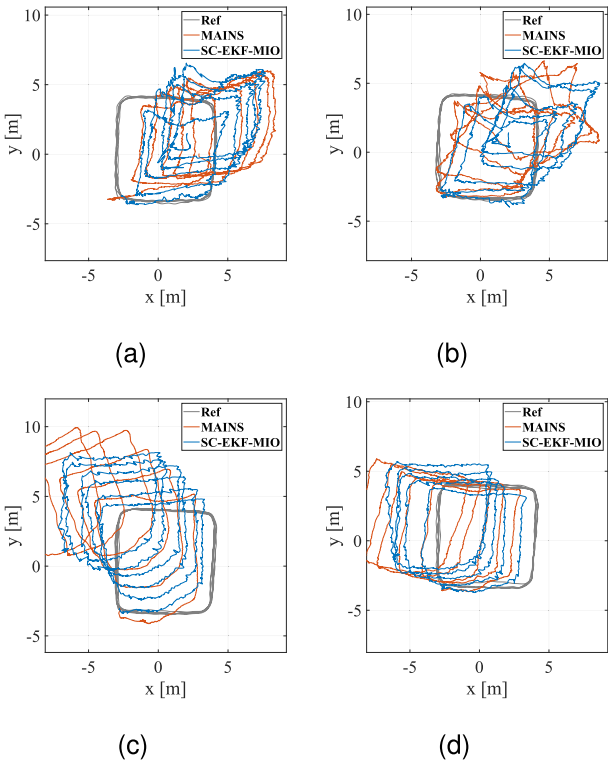

Fig. 9. Localization results for the remaining public datasets. (a) NP-1. (b) NP-3. (c) NT-1. (d) NT-2.

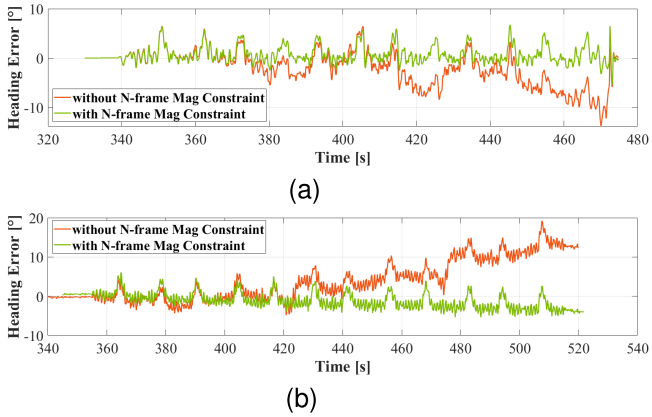

Fig. 10. Comparison of heading angle errors with and without magnetic-vector constraint. (a) aL-1. (b) aM-1.

this section designs a comparative experiment based on the acquired reference attitude of indoor trajectories. In the SC-EKF-MIO solution process, the magnetic-vector constraint is first disabled and then enabled, and the calculated heading angles are compared with the reference heading angles. The rms values of the heading angle deviations are statistically analyzed. Fig. 10 presents the heading angle error comparisons for two datasets, aL-1 and aM-1, and Table V provides the corresponding rms statistics of heading angle errors.

As shown in Fig. 10, the heading angle error exhibits significant temporal divergence when the magnetic-vector constraint is disabled. By the end of the trajectory, the maximum heading deviation approaches 40°. This phenomenon confirms that the heading angle in MIO remains in an unobservable state in the absence of absolute heading references. In contrast, enabling the magnetic constraint substantially reduces the divergence rate of heading errors. According to the statistical metrics in

Table V, the rms heading error remains consistently below 2°. These results demonstrate that introducing the magnetic-vector constraint effectively mitigates heading drift under unobservability conditions. The average rms heading error decreases from 9.8° to 1.80°, achieving an approximately 70% improvement in heading estimation accuracy. By exploiting the slow spatial variation of magnetic disturbances, the algorithm establishes relative constraints on the navigation-frame magnetic-field vectors. The results demonstrate that the proposed method not only mitigates the impact of magnetic interference but also delivers more reliable positioning and heading estimation. This notable improvement arises from the cube relationship governing magnetic-field attenuation with distance [30]. Consequently, magnetic disturbances vary only minimally over small spatial extents and change gradually over larger areas. In typical indoor environments, the magnetic field does not exhibit abrupt fluctuations, thereby ensuring the validity of the magnetic-vector constraint.

E. Analysis of the Impact of Magnetic-Field Gradients

The proposed algorithm utilizes a magnetometer array to measure spatial magnetic gradient variations and constructs constraint information based on the relationship between local gradient changes and the platform's pose. Consequently, significant magnetic gradient variations in the localization environment are critical for the performance of MIO. Due to the cubic decay of magnetic-field intensity with distance, this experiment controls the prominence of magnetic gradients by adjusting the sensor platform's height above the indoor ground. Furthermore, the impact of different gradient magnitudes on odometry performance is analyzed.

Fig. 11 presents normalized magnetic-field magnitude maps at three different heights: low (0.4 m), medium (0.6 m), and nominal (0.8 m). Fig. 12 displays velocity estimation results at varying heights within the same indoor environment. Table VI lists the corresponding rms velocity estimation errors, and Fig. 13 shows the rms error variation with height across the dataset.

It is clearly observable from Fig. 11 that, as the measurement height increases, the magnetic-field magnitude becomes noticeably smoother. Correspondingly, the velocity estimation error plots for the three height levels show that, as the magnetic-field gradient diminishes, the algorithm's error fluctuations increase. The rms statistics of the velocity error demonstrate that the significance of the field gradient has a decisive impact on algorithm performance: at the low height (0.4 m), the mean velocity error rms is only 0.075 m/s; at the medium height (0.6 m), it rises to 0.135 m/s; and at the normal height (0.8 m), it further increases to 0.17 m/s. Nonetheless, even at the normal height, SC-EKF-MIO achieves a velocity error rms that is substantially lower than MAINS's 0.34–0.35 m/s.

The degradation in performance with decreasing magnetic-field significance can be explained as follows. In a magnetometer array, the corrective information primarily arises from the sensitivity of the magnetic measurements to changes in position and orientation. As height increases, the spatial gradient of the magnetic-field weakens, meaning that the same

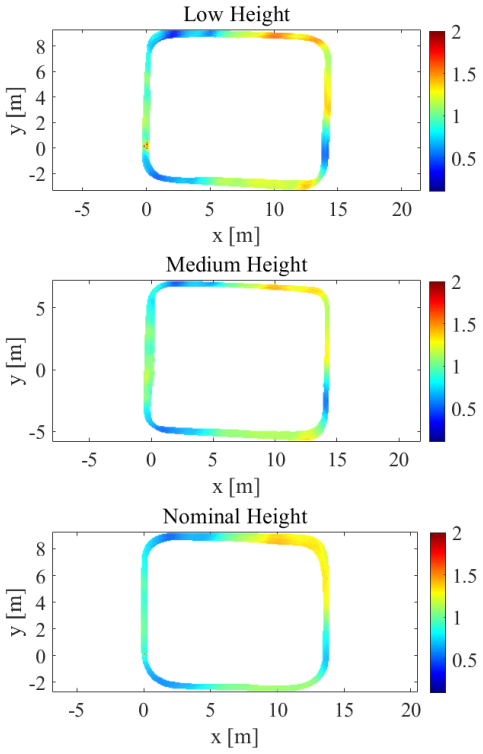

Fig. 11. Magnetic-field magnitude maps at low, medium, and nominal heights.

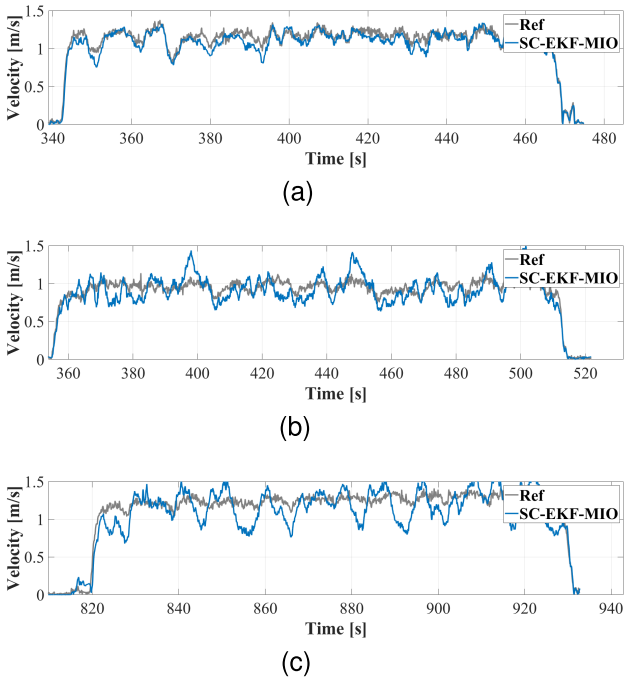

Fig. 12. Velocity estimation results at varying heights in the same indoor environment. (a) aL-1. (b) aM-1. (c) aN-1.

platform displacement induces smaller magnetic differences, which in turn lowers the signal-to-noise ratio of the magnetometer readings. The filter, therefore, struggles to extract effective corrections from these weak-gradient observations, degrading state-estimation performance.

Moreover, this analysis of the magnetic-field gradient also explains why both MAINS and SC-EKF-MIO exhibit pronounced position and heading drift in the public dataset results

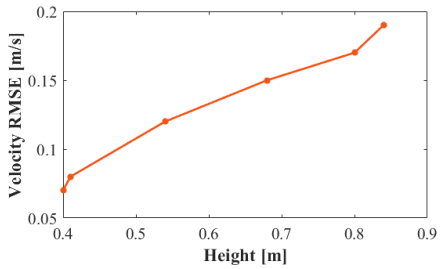

Fig. 13. Velocity error versus height.

shown in Fig. 9: the data were collected at an average height of 0.80 m, where the field attenuation is significant, leading to an overall decline in estimation accuracy. As shown in Fig. 13, the velocity RMSE increases synchronously with the rising average height of the dataset, which effectively illustrates the performance characteristics of the magnetic array inertial odometry during application.

F. Analysis of the Stochastic Cloning Sliding-Window Length

As noted in Section II-B, the theoretical basis of this work rests on the assumption that the local magnetic-field parameters remain invariant within a sufficiently small spatiotemporal neighborhood. This implies that the local magnetic-field model has a limited region of validity. The SC-EKF used here maintains m historical states within a sliding window. The information carried by these m historical states is combined with current observations to construct relative pose constraints. The choice of m determines the temporal length of the sliding window, and consequently, the proposed method is sensitive to the selected value of m. In the following, we analyze the effect of the cloned-state window length using the public dataset.

As described in Section III-C, dt denotes the time interval between two consecutive magnetometer array update steps and, equivalently, the time interval between cloned states. Hence, the cloned-state window length corresponding to a given m is $T = m \cdot dt$. In the open dataset experiments, dt is fixed at 0.05 s. Therefore, the analysis is performed by varying m.

Table VII reports the error statistics for three public datasets under different values of m. The minimum value in each row is highlighted in bold. The results indicate that $m = 2$ yields the best performance across all statistical metrics for the three datasets, and shows a clear improvement over $m = 1$. When only a single cloned state is retained, the historical information available to build relative pose constraints is limited, which increases the variance of the estimates. Moreover, $m = 1$ implies that filter updates occur at shorter time intervals. Because IMU errors are small over short intervals, the state estimate becomes relatively more susceptible to noise in the magnetometer array observations. With $m = 2$, more relative pose information is included, strengthening the observational constraints and thereby significantly reducing the influence of IMU integration errors on position.

However, when m is increased further, performance gradually degrades. On one hand, a larger m extends the spatiotemporal span covered by the cloning window. If the span exceeds the applicability region of the local magnetic-field model, the model can no longer be approximated as invariant over the longer interval, producing biased observations. On the other hand, an excessively long window degrades the system's dynamic responsiveness and imposes a substantially higher computational burden.

Beyond the considerations above, because the effective region of the local magnetic-field model is fundamentally spatial, the choice of m should also account for the platform's motion velocity. For faster platforms, e.g., vehicles, an appropriate adjustment strategy is to reduce m while keeping dt unchanged, or to reduce dt so that, for the same number of cloned states m, the total window length T is smaller.

V. Conclusions and Future Work

In this article, we have presented SC-EKF-MIO, a stochastic-cloning-based MIO method. By leveraging a magnetometer array to observe a local magnetic-field model and estimating its temporal variations, we infer the platform's absolute velocity and use it to correct the position, velocity, and attitude obtained from IMU integration. To address the unobservability of absolute heading, the algorithm incorporates constraints on differences between magnetic-field vectors, successfully improving heading estimation accuracy and thereby enhancing overall positioning precision. Experimental results demonstrate that SC-EKF-MIO achieves high positioning accuracy in environments with pronounced magnetic-field gradients. Under comparable sensor configurations, our method outperforms MAINS in both velocity and attitude estimation. Notably, SC-EKF-MIO requires neither motion assumptions nor a prior magnetic-fingerprint database, offering a low-power, low-cost, and reliable solution for non-cooperative indoor platforms, especially pedestrian or tunnel navigation, under no-prior-information conditions. However, this performance is contingent on the presence of pronounced magnetic-field gradient features in the environment.

Future work will focus on evaluating algorithm performance in environments where the magnetic-field gradient is weak. One promising direction is to integrate magnetic-sequence waveform matching to bolster velocity estimation when field gradients are minimal. Moreover, for pedestrian-tracking applications, one could leverage measurements from sensors mounted on other body segments to generate additional constraints, thereby establishing a cooperative, body-sensor-network framework for collaborative localization.

References

[1] S. A. S. Mohamed, M.-H. Haghbayan, T. Westerlund, J. Heikkonen, H. Tenhunen, and J. Plosila, "A survey on odometry for autonomous navigation systems," *IEEE Access*, vol. 7, pp. 97466–97486, 2019.

[2] B.-S. Cho, W.-S. Moon, W.-J. Seo, and K.-R. Baek, "A dead reckoning localization system for mobile robots using inertial sensors and wheel revolution encoding," *J. Mech. Sci. Technol.*, vol. 25, no. 11, pp. 2907–2917, Nov. 2011.

[3] S. Du, W. Sun, and Y. Gao, "MEMS IMU error mitigation using rotation modulation technique," *Sensors*, vol. 16, no. 12, p. 2017, Nov. 2016.

[4] R. Gonzalez, F. Rodriguez, J. L. Guzman, C. Pradalier, and R. Siegwart, "Control of off-road mobile robots using visual odometry and slip compensation," *Adv. Robot.*, vol. 27, no. 11, pp. 893–906, Aug. 2013.

[5] J. Horn and G. Schmidt, "Continuous localization of a mobile robot based on 3D-laser-range-data, predicted sensor images, and dead-reckoning," *Robot. Auto. Syst.*, vol. 14, nos. 2–3, pp. 99–118, May 1995.
[6] C. Xue et al., "A Gaussian-generalized-inverse-Gaussian joint-distribution-based adaptive MSCKF for visual-inertial odometry navigation," *IEEE Trans. Aerosp. Electron. Syst.*, vol. 59, no. 3, pp. 2307–2328, Jun. 2023.
[7] H. Zhang, D. Wang, and J. Huo, "A visual-inertial dynamic object tracking SLAM tightly coupled system," *IEEE Sensors J.*, vol. 23, no. 17, pp. 19905–19917, Sep. 2023.
[8] H. Zhang, D. Wang, and J. Huo, "Real-time dynamic SLAM using moving probability based on IMU and segmentation," *IEEE Sensors J.*, vol. 24, no. 7, pp. 10878–10891, Apr. 2024.
[9] H. Zhang, J. Huo, Y. Huang, and Q. Liu, "Real-time dynamic visual-inertial SLAM and object tracking based on lightweight deep feature extraction matching," *IEEE Trans. Instrum. Meas.*, vol. 74, pp. 1–22, 2025.
[10] C. Huang, G. Hendeby, H. Fourati, C. Prieur, and I. Skog, "MAINS: A magnetic-field-aided inertial navigation system for indoor positioning," *IEEE Sensors J.*, vol. 24, no. 9, pp. 15156–15166, May 2024.
[11] D. Vissiere, A. Martin, and N. Petit, "Using distributed magnetometers to increase IMU-based velocity estimation into perturbed area," in *Proc. 46th IEEE Conf. Decis. Control*, Jun. 2007, pp. 4924–4931.
[12] D. Vissière, A. Martin, and N. Petit, "Using magnetic disturbances to improve IMU-based position estimation," in *Proc. Eur. Control Conf. (ECC)*, Jul. 2007, pp. 2853–2858.
[13] P. Batista, N. Petit, C. Silvestre, and P. Oliveira, "Further results on the observability in magneto-inertial navigation," in *Proc. Amer. Control Conf.*, Jun. 2013, pp. 2503–2508.
[14] E. Dorveaux, "Magneto-inertial navigation: Principles and application to an indoor pedometer," Ph.D. dissertation, Dept. Math. Control, École Nationale Supérieure des Mines de Paris, Paris, France, 2011.
[15] C.-I. Chesneau, M. Hillion, and C. Prieur, "Motion estimation of a rigid body with an EKF using magneto-inertial measurements," in *Proc. Int. Conf. Indoor Positioning Indoor Navigat. (IPIN)*, Oct. 2016, pp. 1–6.
[16] L. Fan, C. Kang, X. Zhang, Q. Zheng, and M. Wang, "An efficient method for tracking a magnetic target using scalar magnetometer array," *SpringerPlus*, vol. 5, no. 1, p. 502, Dec. 2016.
[17] L.-M. Fan, Q. Zheng, X.-Y. Kang, X.-J. Zhang, and C. Kang, "Baseline optimization for scalar magnetometer array and its application in magnetic target localization," *Chin. Phys. B*, vol. 27, no. 6, Jun. 2018, Art. no. 060703.
[18] M. Zmitri, H. Fourati, and C. Prieur, "Improving inertial velocity estimation through magnetic field gradient-based extended Kalman filter," in *Proc. Int. Conf. Indoor Positioning Indoor Navigat. (IPIN)*, Sep. 2019, pp. 1–7.
[19] I. Skog, G. Hendeby, and F. Gustafsson, "Magnetic odometry—A model-based approach using a sensor array," in *Proc. 21st Int. Conf. Inf. Fusion (FUSION)*, Jul. 2018, pp. 794–798.
[20] C. Huang, G. Hendeby, and I. Skog, "A tightly-integrated magnetic-field aided inertial navigation system," in *Proc. 25th Int. Conf. Inf. Fusion (FUSION)*, Jul. 2022, pp. 1–8.
[21] T. Zhang, L. Wei, J. Kuang, H. Tang, and X. Niu, "Mag-ODO: Motion speed estimation for indoor robots based on dual magnetometers," *Measurement*, vol. 222, Nov. 2023, Art. no. 113688.
[22] Y. Liu, W. Zhang, L. Cao, and D. Wei, "Ped-Mag-ODO: Indoor pedestrian motion speed estimation method based on dual magnetometers," *IEEE Internet Things J.*, vol. 12, no. 8, pp. 10627–10639, Aug. 2024.
[23] J. Kuang, X. Niu, and X. Chen, "Robust pedestrian dead reckoning based on MEMS-IMU for smartphones," *Sensors*, vol. 18, no. 5, p. 1391, May 2018.
[24] S. I. Roumeliotis and J. W. Burdick, "Stochastic cloning: A generalized framework for processing relative state measurements," in *Proc. IEEE Int. Conf. Robot. Autom.*, vol. 2, Washington, DC, USA, Jul. 2002, pp. 1788–1795.
[25] J. A. Hesch, D. G. Kottas, S. L. Bowman, and S. I. Roumeliotis, "Consistency analysis and improvement of vision-aided inertial navigation," *IEEE Trans. Robot.*, vol. 30, no. 1, pp. 158–176, Feb. 2014.
[26] Y. Wu, D. Zou, P. Liu, and W. Yu, "Dynamic magnetometer calibration and alignment to inertial sensors by Kalman filtering," *IEEE Trans. Control Syst. Technol.*, vol. 26, no. 2, pp. 716–723, Mar. 2018.
[27] J. Kuang, T. Liu, Y. Wang, X. Meng, and X. Niu, "Magnetic vector constraint pedestrian dead reckoning based on foot-mounted and waist-mounted IMU," *IEEE Internet Things J.*, vol. 12, no. 10, pp. 14538–14547, May 2025.
[28] T. Edridge and M. Kok, "Position and orientation estimation uncertainty using magnetometer arrays for indoor localization," *IEEE J. Indoor Seamless Positioning Navigat.*, vol. 3, pp. 152–164, 2025.
[29] W. Xu, Y. Cai, D. He, J. Lin, and F. Zhang, "FAST-LIO2: Fast direct LiDAR-inertial odometry," *IEEE Trans. Robot.*, vol. 38, no. 4, pp. 2053–2073, Aug. 2022.
[30] K. P. Subbu, B. Gozick, and R. Dantu, "LocateMe: Magnetic-fields-based indoor localization using smartphones," *ACM Trans. Intell. Syst. Technol.*, vol. 4, no. 4, pp. 1–27, 2013.

Jiazhu Li received the B.Eng. degree in navigation engineering from Wuhan University, Wuhan, China, in 2024, where he is currently pursuing the master's degree in navigation, guidance, and control.

His research interests include inertial navigation, sensor fusion algorithms, and the construction of crowdsourced indoor pedestrian localization fingerprint libraries.

Jian Kuang received the B.Eng. and Ph.D. degrees (Hons.) in geodesy and survey engineering from Wuhan University, Wuhan, China, in 2013 and 2019, respectively.

He is currently an Associate Professor with the GNSS Research Center, Wuhan University. His research interests include magnetic field-based navigation, inertial navigation, pedestrian navigation, and indoor positioning.

Yan Wang received the B.Eng. degree in chemical engineering and technology and the M.S. degree in computer applied technology from China University of Mining and Technology, Xuzhou, China, in 2016 and 2019, respectively, and the Ph.D. degree from Wuhan University, Wuhan, China, in 2023.

He is currently a Post-Doctoral Researcher with Wuhan University. His research concentration lies in indoor navigation, sensor fusion algorithms, and computer vision.

Xiaoji Niu (Member, IEEE) received the bachelor's and Ph.D. degrees (Hons.) from the Department of Precision Instruments, Tsinghua University, Beijing, China, in 1997 and 2002, respectively.

He was a Post-Doctoral Researcher at the University of Calgary, Calgary, AB, Canada, and worked as a Senior Scientist at SiRF Technology Inc., San Jose, CA, USA. He is currently a Professor at the GNSS Research Center, Wuhan University, Wuhan, China. He is also leading the Integrated and Intelligent Navigation (i2Nav) Group, Wuhan University. He has published 200+ academic papers and owns 50+ patents. His research interests focus on GNSS/INS integration, low-cost navigation sensor fusion, and relevant new applications.